



**HAL**  
open science

## Solar calcination at pilot scale in a continuous flow multistage horizontal fluidized bed

Thibaut Esence, Emmanuel Guillot, Michael Tessonnaud, Jean-Louis Sans,  
Gilles Flamant

► **To cite this version:**

Thibaut Esence, Emmanuel Guillot, Michael Tessonnaud, Jean-Louis Sans, Gilles Flamant. Solar calcination at pilot scale in a continuous flow multistage horizontal fluidized bed. *Solar Energy*, 2020, 207, pp.367 - 378. 10.1016/j.solener.2020.06.098 . hal-03523228

**HAL Id: hal-03523228**

**<https://univ-perp.hal.science/hal-03523228>**

Submitted on 18 Jul 2022

**HAL** is a multi-disciplinary open access archive for the deposit and dissemination of scientific research documents, whether they are published or not. The documents may come from teaching and research institutions in France or abroad, or from public or private research centers.

L'archive ouverte pluridisciplinaire **HAL**, est destinée au dépôt et à la diffusion de documents scientifiques de niveau recherche, publiés ou non, émanant des établissements d'enseignement et de recherche français ou étrangers, des laboratoires publics ou privés.



Distributed under a Creative Commons Attribution - NonCommercial 4.0 International License

1  
2  
3  
4  
5  
6  
7  
8  
9  
10

## Solar calcination at pilot scale in a continuous flow multistage horizontal fluidized bed

Thibaut Esence, Emmanuel Guillot, Michael Tessonnaud, Jean-Louis Sans, Gilles Flamant\*

Processes, Materials and Solar Energy laboratory, PROMES-CNRS

7, rue du Four solaire, 66120 Font Romeu, France

\*Corresponding author, [gilles.flamant@promes.cnrs.fr](mailto:gilles.flamant@promes.cnrs.fr)

### Abstract

Calcination of limestone for lime production was successfully performed in the continuous flow mode on a daily basis in a fluidized bed indirectly heated by concentrated solar radiation. Industrial calcium carbonate feedstock was decomposed at the focus of the CNRS 1 MW solar furnace in a pilot-scale solar reactor operating at an average power of 55 kW. The reactor was a four-stage horizontal fluidized bed, irradiated on a front metallic wall of 1 m long and 0.4 m high. A novel aiming strategy was applied to reduce the hot spots on the irradiated wall. The conversion degree was analyzed as a function of the fluidization conditions (air mass flow rate) and the particle mass flow rate. This latter parameter varied in range (14.5 – 25 kg/h), and the highest conversion degrees were obtained at high fluidization velocity. The best result was obtained for a calcite mass flow rate of 20 kg/h, resulting in a degree of conversion of 95.2%, a BET surface area of the lime of 5.39 m<sup>2</sup>/g, and 17% and 29% thermochemical and thermal efficiencies of the reactor, respectively. This achievement corresponds to a particle mass flow rate three times higher than the current state of the art for solar calcination of lime.

### Keywords

Solar calcination; fluidized bed reactor; pilot-scale continuous operation; solar thermochemistry; quicklime, solar heat in energy-intensive industry

## 28 1. Introduction

29 Calcination is an emblematic chemical reaction in solar thermochemistry for many reasons.  
30 First, it is a representative reaction of energy-intensive industry as well as lime and cement  
31 production, which is responsible for approximately 7-8% of worldwide anthropogenic CO<sub>2</sub>  
32 emissions (Olivier et al., 2016). Second, calcination occurs at 800-900 °C, a temperature level  
33 that corresponds to the optimum operation temperature of point-focusing systems with a mean  
34 concentration of 1000 (Fletcher and Moen, 1977; Li et al., 2016). Third, calcination is a solid-  
35 gas reaction that necessitates the processing of specific reactor developments with solar  
36 energy.

37 In the lime industry, limestone is processed to produce lime in two main reactor types, shaft  
38 kilns and rotary kilns (EuLA, 2020). Shaft kilns are vertical kilns that operate in the moving  
39 packed-bed mode. The limestone being processed is fed from a top hopper in a vertical  
40 chamber in which the static bed moves downward in plug flow. The particle diameters range  
41 from 20 mm to 175 mm. Twin shaft parallel flow regenerative kilns are composed of two  
42 interconnected shafts fired in sequence to achieve excellent energy efficiency; the particle  
43 diameters are usually between 90 mm and 125 mm. Rotary kilns are rotating cylinders inclined  
44 at an angle of 3 to 4 degrees horizontally. They process particle sizes in the 15 – 40 mm range.  
45 They are fueled by coal, petroleum coke, natural gas, and waste-derived fuels. In contrast,  
46 twin shaft kilns that produce high-purity and high-reactivity quicklime are fueled with natural  
47 gas. Single-chamber shaft kilns can be operated on natural gas as well as liquid and solid  
48 fuels. Fluidized beds are marginally used in the lime industry for highly reactive products.

49 In traditional processes, the heat of reaction is supplied by combustion of carbon-based fuels.  
50 Under these conditions, approximately 40% of the total CO<sub>2</sub> emissions from lime production  
51 are related to combustion; the rest is due to chemical reaction. Consequently, replacing fossil  
52 combustion with renewable energy in limestone calcination can result in 40% reduction of CO<sub>2</sub>  
53 emissions. One possible option is using biomass, either solid or gas, as a heat source. The  
54 main advantage of this choice is the ability to operate existing kilns in continuous mode using  
55 this fuel. Nevertheless, burning biomass prevents the increase of this feedstock's value with  
56 the synthesis of carbon-based chemicals and fuels. Moreover, solid biomass contains minerals  
57 (Na, K, Si, P...) that can pollute the lime. Concentrated solar energy can provide high  
58 temperatures without producing any additional byproducts, thereby offering a renewable option  
59 for the production of high-quality lime.

60 The development of solar calcination started more than forty years ago with the demonstration  
61 of batch calcium carbonate decomposition in lab-scale solar fluidized beds and rotary kilns  
62 (Flamant et al. 1980). However, the development of solar fluidized-bed reactors (Tregambi et  
63 al., 2018) never achieved both continuous operation and pilot scale. Vortex-type reactors, such

64 as cyclones, have been developed to process small particles (diameter typically less than  
65 10  $\mu\text{m}$ ) in continuous-flow solar reactors (Imhof, 2000, 1997; Nikulshina et al., 2009; Steinfield  
66 et al., 1991). Solar rotary kilns were demonstrated at the power level of approximately 10-15  
67 kW in both indirect-heating configurations (Meier et al., 2006) and direct-heating configurations  
68 (Moumin et al., 2019). Meier et al. (2006) processed 1–5 mm limestone particles in an indirectly  
69 heated 10 kW<sub>th</sub> multitube rotary kiln prototype. The best result reflected a lime production of  
70 3.85 kg/h (6.88 kg/h limestone) with a conversion degree of 98% and a thermochemical  
71 efficiency of 34.8%; the maximum measurement uncertainty was estimated as  $\pm 15.2\%$ . This  
72 previous research addressed large particles (mean diameter larger than 1 mm). In contrast,  
73 the recent developments of Moumin et al. (2019) dealt with the calcination of fine cohesive  
74 particles in a rotary kiln. They performed the calcination of cement raw meal (particle-size  
75 distribution in the range of 1–176  $\mu\text{m}$ , with 50% smaller than 15  $\mu\text{m}$ ) with a conversion degree  
76 of up to 99%. This latter value was achieved for a 4 kg/h feedstock mass flow rate,  
77 corresponding to a thermochemical efficiency and an overall efficiency of approximately 10  
78 and 20%, respectively.

79 Esence et al. (2020) demonstrated the concept of a solar horizontal fluidized bed for the first  
80 time at lab scale for the continuous calcination of dolomite. The half decomposition of a  
81 continuous stream of 9.4 kg/h dolomite ( $\text{CaMg}(\text{CO}_3)_2 \rightarrow \text{CaCO}_3 + \text{MgO} + \text{CO}_2$ ) was performed  
82 with a conversion degree of 100%. The measured thermochemical efficiency was 6.6%.

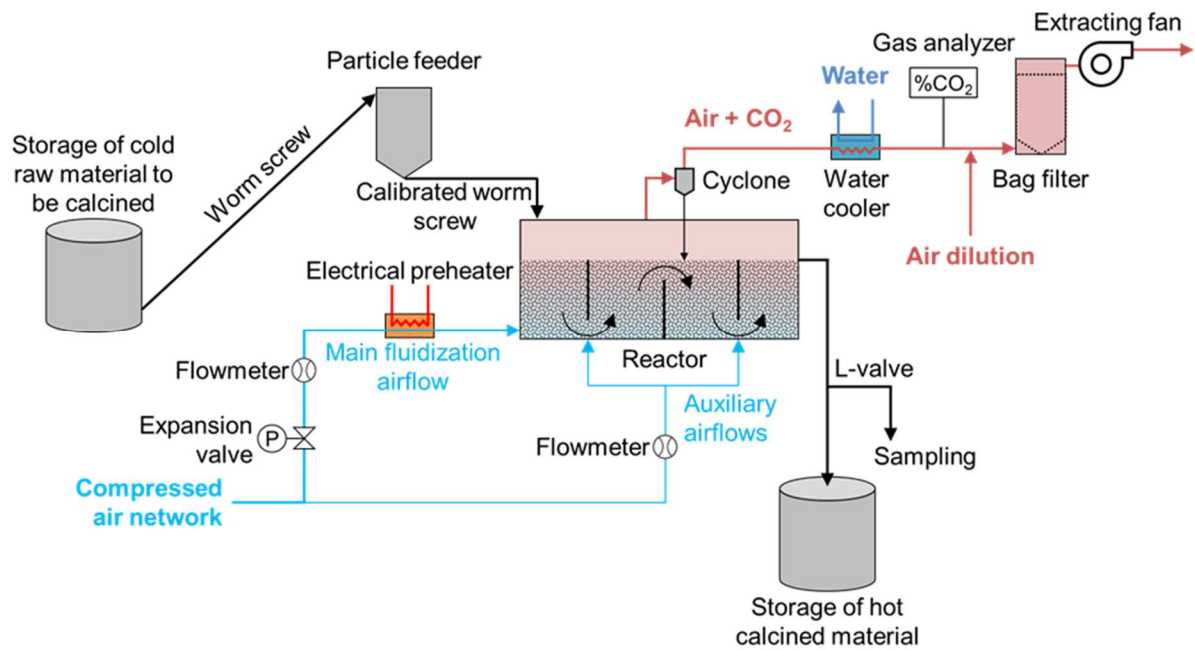
83 Accounting for the previous state of the art, this paper presents the development of solar  
84 horizontal fluidized bed technology at pilot scale (45-65 kW<sub>th</sub>) for the continuous processing of  
85 limestone, which has never been demonstrated in a solar fluidized bed to date. The other  
86 objective of the work was to demonstrate solar calcination of limestone with a mass flow rate  
87 greater than 10 kg/h. The solar reactor and the aiming strategy are presented in the next  
88 section. Then, the experimental results are examined with a detailed analysis of the influence  
89 of process parameters on the conversion degree. Finally, the product quality and the reactor  
90 performance are analyzed.

91

## 92 **2. Experiment**

93 The complete experimental setup was implemented at the focus of the CNRS 1 MW-solar  
94 furnace. It was composed of a cavity reactor, a particle-feeding device, a particle sampling  
95 system, and an exhaust gas treatment, including a CO<sub>2</sub> analyzer and pressurized air  
96 distribution system, as illustrated in Figure 1.

97



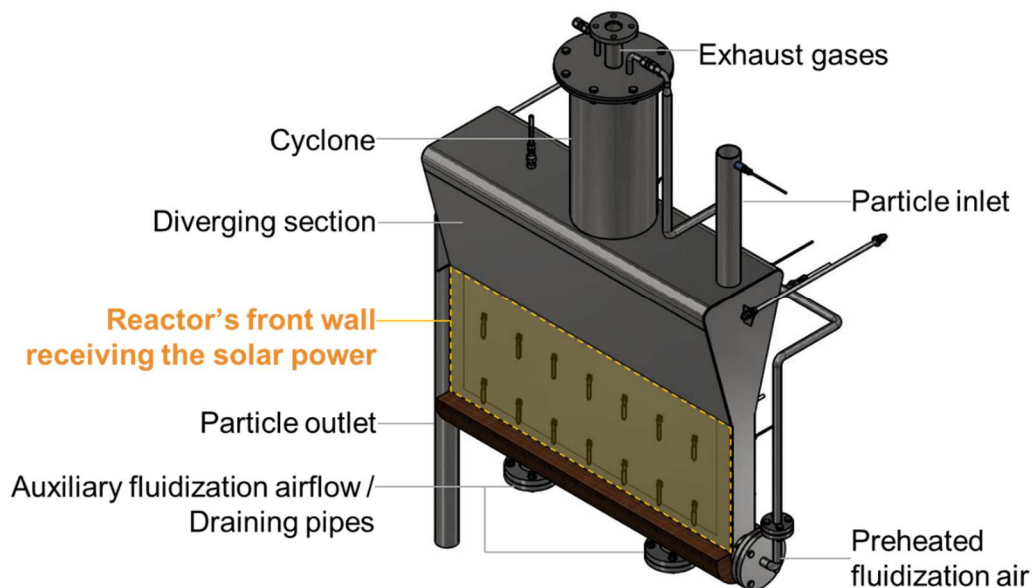
98

99 **Figure 1.** Schematic of the complete experimental continuous calcination setup installed at the focus  
 100 of the 1-MW CNRS solar furnace.

101 The next sections describe the main components of the experimental setup.

102 *Solar receiver-reactor*

103 The solar receiver-reactor was composed of the reactor itself acting as a solar absorber and  
 104 the cavity where it was located. The key component was the fluidized-bed reactor depicted in  
 105 Figure 2. The reactor was a multistage horizontal fluidized bed manufactured by COMESSA.



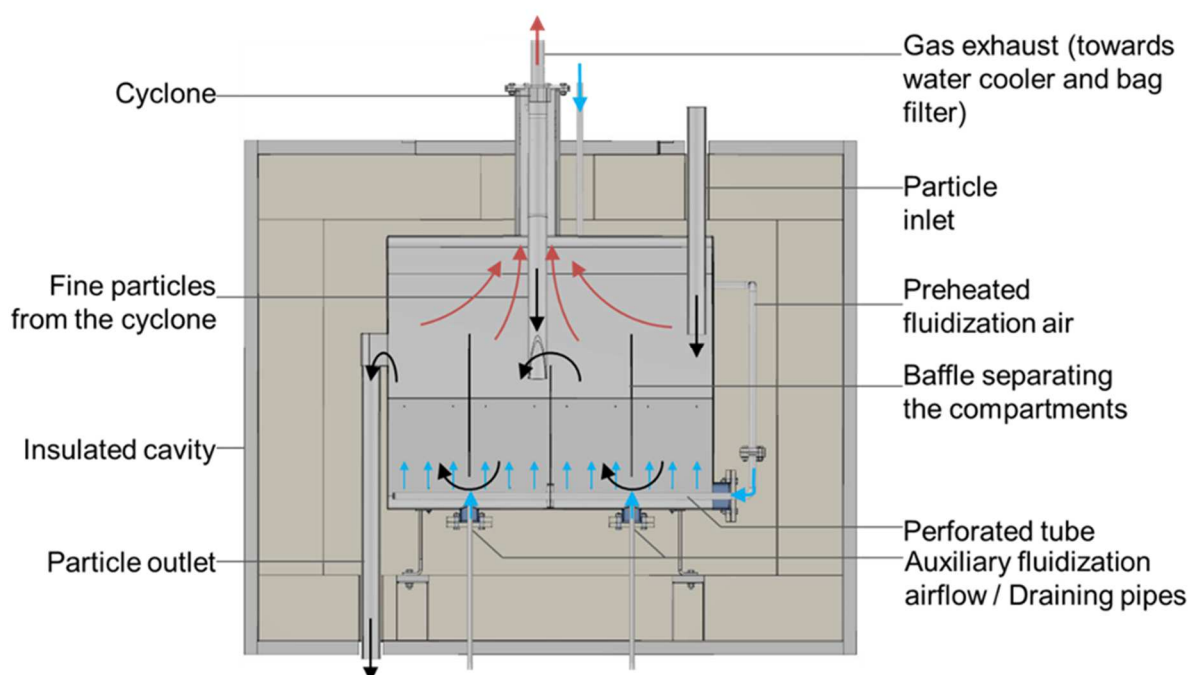
106

107 **Figure 2.** The pilot-scale solar reactor.

108 The reactor was built in Incoloy® 800HT (nickel 32%, chromium 20%, iron 48%) that can  
 109 sustain temperatures up to 1100 °C. It was 1-m long and had an internal width of 8 cm. It  
 110 consisted of four 25 cm-long compartments in series in which the fluidized particles were  
 111 heated with solar energy to carry out the calcination reaction.

112 During operation, the front wall was irradiated and heated by concentrated solar flux. The heat  
 113 absorbed by the front wall was transferred to the fluidized particles circulating in the reactor by  
 114 conduction, convection and radiation. The concentrated solar energy provided the sensible  
 115 heat and the reaction enthalpy required to perform the endothermic calcination reaction. The  
 116 front wall of the reactor was initially coated with high-temperature paint, Pyromark® 2500, in  
 117 order to improve its optical properties (increase the solar absorptivity and decrease the infrared  
 118 emissivity). After several hours of operation, the paint was degraded by the concentrated solar  
 119 flux and was naturally replaced by metallic oxides (especially chromium oxide) produced by  
 120 the accelerated aging of the reactor. This was not an issue because the metallic oxides have  
 121 high solar absorptivity at high temperatures,  $\alpha > 0.80$  (Touloukian and Dewitt, 1970).

122 The particles were introduced into the first compartment of the reactor from the top. Due to  
 123 fluidization, the bed of particles behaved as a fluid and overflowed by gravity from one  
 124 compartment to the other until the outlet tube at the end of the fourth compartment was reached  
 125 (see Fig. 3). The baffles between the compartments and the outlet of the reactor were designed  
 126 so that the average height of the fluidized bed was 40 cm. This corresponded to a fluidized  
 127 bed volume of 35 L, i.e., approximately 48 kg of particles (assuming a density of 2700 kg/m<sup>3</sup>  
 128 and a void fraction of 0.5). Above the 40 cm height, a disengaging zone (conical part in Fig. 2)  
 129 limited the particle entrainment. The particles leaving the reactor overflowed into the outlet  
 130 tube, which was connected either to a storage tank or to a sampling vessel.



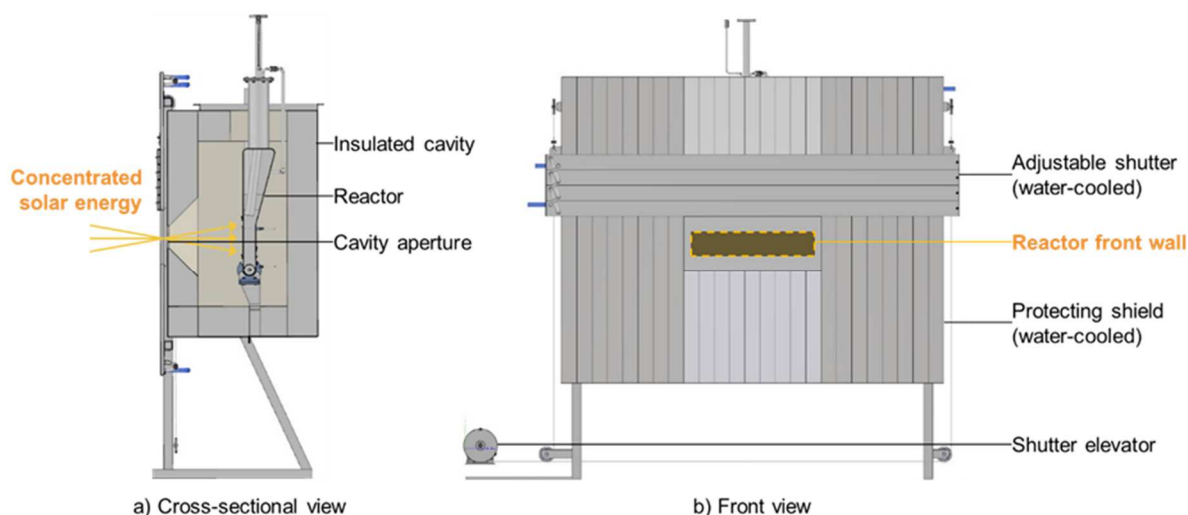
131

132 **Figure 3.** Cross-sectional view of the reactor-receiver inserted inside the cavity with principle of  
133 particle and gas flows (— particles; — fluidization air; — exhaust gases).

134 The fluidizing airflow was electrically preheated and then injected through a perforated tube  
135 located at the bottom of the reactor. In addition, two auxiliary airflows at ambient temperature  
136 were injected below the baffles of the first two and the last two compartments. These auxiliary  
137 airflows facilitated the circulation of the particles below the baffles.

138 The hot fluidization air and the carbon dioxide produced by the reaction were extracted at the  
139 top of the reactor. They first passed through the disengaging section, which reduced the gas  
140 velocity and hence the amount of entrained particles. The gases then passed through an  
141 internal cyclone that separated the gas and the remaining fine particles. As the fine particles  
142 fell back into the reactor, the gas (mixture of air and carbon dioxide) was extracted from the  
143 reactor.

144 The reactor was located in a cavity insulated with ceramic fiber (see Fig. 4-a). The cavity  
145 improved the thermal efficiency of the system by reducing the radiative and convective heat  
146 losses. A water-cooled aluminum panel protected the cavity from spilled concentrated solar  
147 energy (see Fig. 4-b). A movable water-cooled aluminum shutter matching the aperture of the  
148 cavity (80 cm x 20 cm) was placed in front of the previous panel. The shutter moved vertically  
149 to vary the size of the aperture and, as a result, to control the solar power entering the cavity.  
150 The opening of the cavity aperture was accurately measured ( $\pm 2$  mm) with a ruler.



151 a) Cross-sectional view  
152 **Figure 4.** Schematic of the solar cavity and the protecting shield. a) Cross-sectional side view. b)  
153 Front view.

154  
155  
156

157 *Gas and particle circuits*

158 The particles were fluidized with air supplied by a compressor. An expander ensured that the  
159 air entered the flowmeter at 0.8 relative bar. Following the flowmeter, the airflow passed  
160 through an electrical preheater regulated to heat the air at 700 °C. Then, the airflow was  
161 injected in the reactor through the fluidization distributor (i.e., the perforated tube). Due to  
162 thermal losses between the preheater and the distributor, the temperature of the air injected in  
163 the reactor was less than 700 °C and depended on the operating conditions and temperature  
164 inside the solar cavity. Electrical heating of the fluidization air was used to hasten the heating  
165 period of the reactor and, consequently, to enable long periods of stable operation every testing  
166 day.

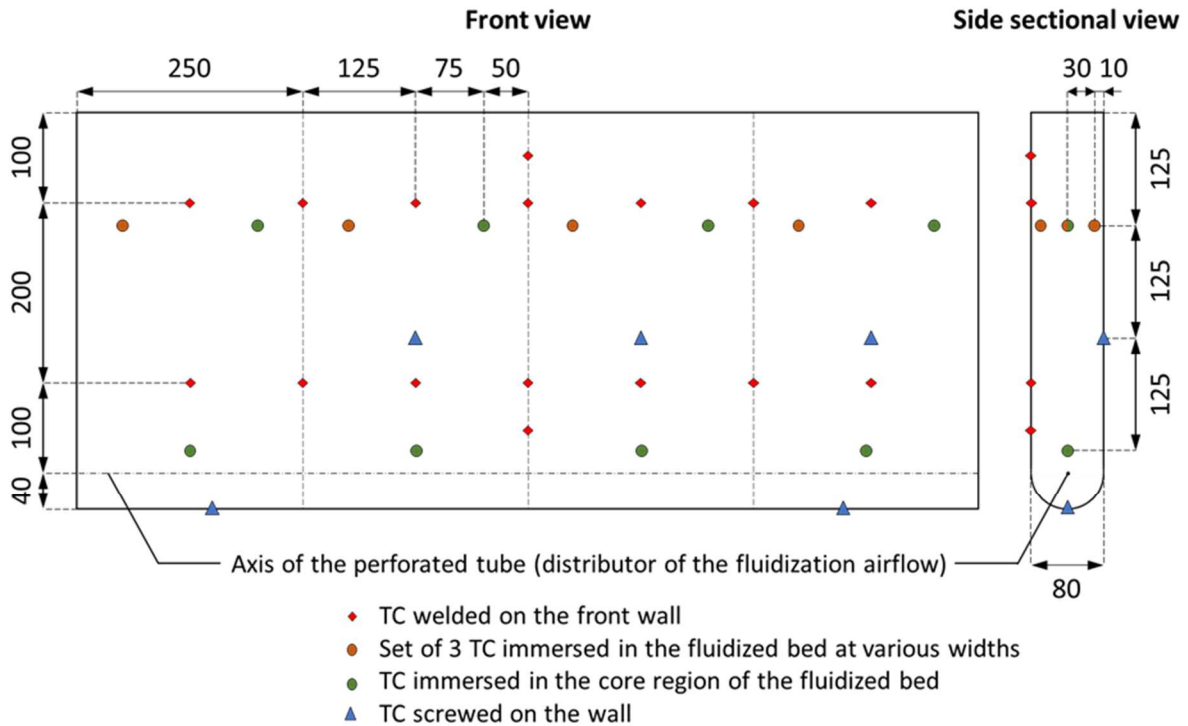
167 The CO<sub>2</sub> and the fluidization air drawn from the reactor and exiting from the cyclone were  
168 cooled down by a water cooler. A gas analyzer measured the CO<sub>2</sub> content in the extracted  
169 gases and enabled monitoring of the calcination reaction. Then, the extracted gases were  
170 diluted with an airflow that further reduced the temperature of the exhaust gases. These gases  
171 were then released into the atmosphere through a bag filter.

172 The particles to be calcined were stored in a large vessel (cold storage). A first worm screw  
173 periodically supplied the reactor feeder with the stored particles. The reactor feeder was  
174 equipped with a second worm screw. A variable speed motor drove the feeder's worm screw  
175 in order to control the mass flow rate of particles entering the reactor. During preliminary tests,  
176 the linear relation between the settings of the speed controller and the mass flow rate of  
177 particles was established. The particles delivered by the feeder fell on a vibrating ramp that  
178 moved the particles towards the reactor inlet. The vibrating ramp was aimed only at  
179 transporting the particles and was not intended to control the particle mass flow rate.

180 *Instrumentation*

181 The whole test loop was equipped with 48 K-type thermocouples. The reactor itself was  
182 equipped with 41 thermocouples (see Fig. 5).

183



184

185 **Figure 5.** Schematic of the reactor showing the position of the thermocouples (dimensions in mm).

186

187 There were 16 thermocouples spot-welded on the front wall of the reactor-receiver (see Fig.  
 188 6). They were mainly used during operation to ensure that overheating did not occur (reactor  
 189 wall should not exceed 1100 °C at any location) and to estimate the wall temperature  
 190 distribution. On the back and at the bottom of the reactor, five thermocouples were screwed in  
 191 and enabled for calculating the energy balance of the reactor. Inside the fluidized bed reactor,  
 192 20 thermocouples were implemented through ports at various depths and widths in each  
 193 compartment in order to strictly monitor the temperature of the fluidized bed, as shown in  
 194 Figure 5. All these thermocouples allowed the determination of a representative average  
 195 temperature of the bed, characterization of the thermal homogeneity of the reactor, and  
 196 measurement of thermal gradients due to heat transfers in the fluidized bed.

197 In addition, thermocouples were located at key points of the loop: in the fluidization air before  
 198 and after preheating, exhaust gas before and after the cooler, fines from the cyclone, and  
 199 particles in the cold and hot tanks.



200

201 **Figure 6.** View of the reactor (left) inside the cavity with the welded thermocouple on the front wall.

202 Right side is the water-cooled aperture and the inner insulation.

203 Five pressure sensors were located at various heights in the reactor. An additional pressure  
204 sensor was located at the inlet of the air distributor in order to calculate the physical properties  
205 of the fluidization air.

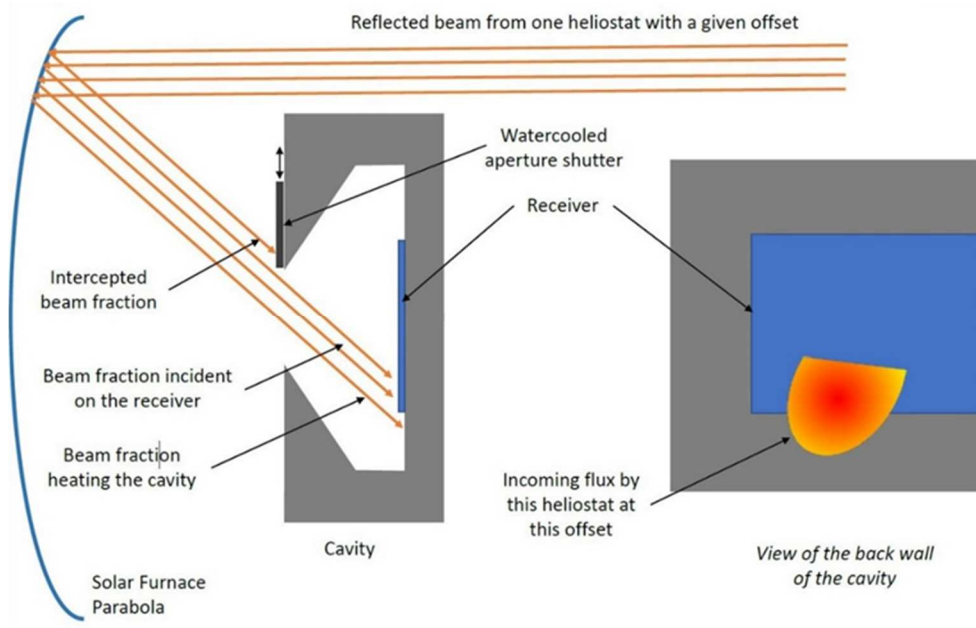
206 The mass flow of the fluidization air was measured by a Kobold KME thermal flow sensor  
207 (accuracy  $\pm 3\%$  of reading +  $\pm 0.6 \text{ sm}^3/\text{h}$ ). The mass flow and the physical properties (pressure  
208 and temperature) of fluidization air determined the average gas velocity in the reactor. It ranged  
209 from 0.15 to 0.40 m/s. The air mass flow was controlled by using a needle valve in order to  
210 reach the set value. Usually, a mass flow corresponding to 5 to 10 times the minimum  
211 fluidization velocity of the particles was set in the reactor.

212 All the measuring instruments were connected to a data logger, Graphtec midi Logger GL800,  
213 that was connected to a laptop. The measuring data were recorded with a frequency of 1 Hz  
214 through a dedicated software developed with LabVIEW.

#### 215 *Control of solar flux distribution, aiming strategy*

216 Ideally, a homogenous incident concentrated flux is delivered by the solar facility to avoid hot  
217 spots on the receiver that would damage or even destroy the reactor. However, as all solar  
218 furnaces, the 1 MW solar furnace was designed to achieve very high peak fluxes on a small  
219 surface, as opposed to a homogenous flux on a large surface, such as the SOLPART receiver.  
220 Each of the 63 heliostats delivers nearly the same power on the focal plane, but their peak flux  
221 density ranges from 15 to 330 suns, and their beam incident angles range from 15 to 75° due  
222 to their relative location in the field compared to the parabola and its optical axis. By aiming  
223 each heliostat at a different location instead of the nominal focal point, these power distribution

224 differences can be used to control the flux distribution on the setup. However, the use of a  
 225 cavity makes it difficult to determine the aiming location, as a small offset of a heliostat at the  
 226 focal plane may move its beam suddenly inside or outside the cavity. The cavity aperture acts  
 227 as an optical diaphragm, or a letterbox, through which the appropriate flux at the appropriate  
 228 location must be controlled (Fig. 7). In addition, the size of the effective aperture may change  
 229 by moving the shutter placed in front of the main cavity aperture.



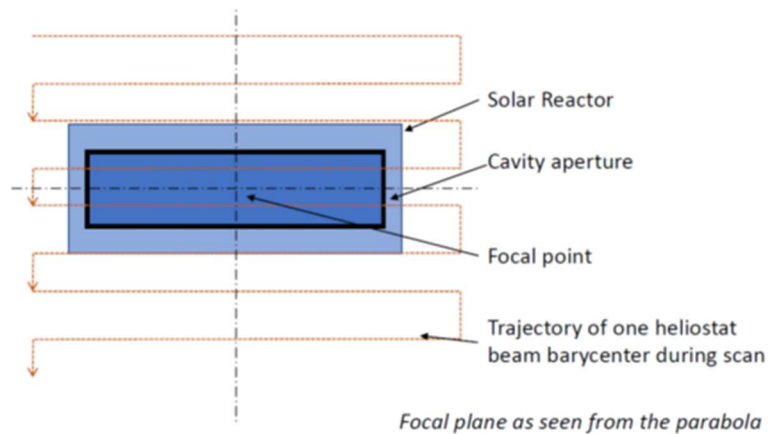
230

231 **Figure 7.** Simplified cross-sectional view with a beam reflected by a heliostat being intercepted by the  
 232 cavity aperture and partially impacting the receiver (left), also seen on the back wall of the cavity  
 233 (right).

234 Notably not depicted here: the additional beam interceptions by the doors of the solar furnace.

235 The problem was solved using a hybrid simulation-experimental method. The flux distribution  
 236 on the reactor front wall for each heliostat at each considered offset location (heliostat flux  
 237 distribution with offsets database) was measured to create a database. Then, a simulation tool  
 238 was created to select the heliostat configurations in this database to reach the targeted mean  
 239 flux density with a given constraint on the minimum and maximum local flux density (to avoid  
 240 hot spots) and the standard flux deviation (to represent homogeneity).

241 To produce the flux distribution database, each heliostat was scanned at the focal plane, and  
 242 the actual flux distribution inside a mockup cavity (a diffusive-reflective target placed at the  
 243 location of the reactor) was measured with a calibrated camera (Fig. 8).



244

245 **Figure 8.** Principle of the scan of each heliostat on the focal plane to build the flux database as a  
 246 function of the heliostat offsets.

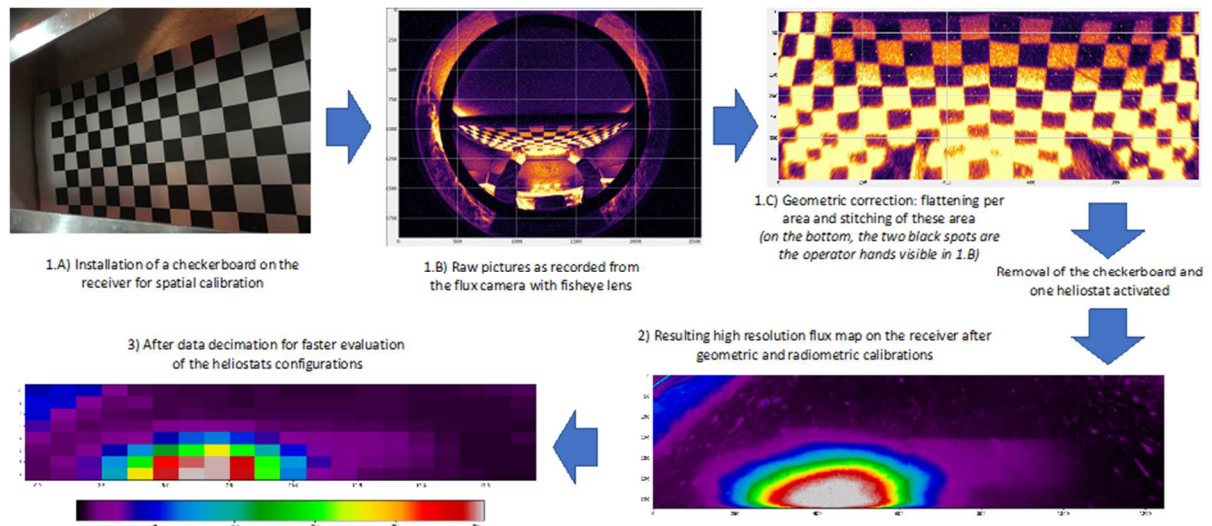
247 The camera-based flux measurement system was adapted in order to cope with the camera  
 248 installed inside the cavity, which used a fisheye lens that produced strong optical aberrations  
 249 requiring adapted correction. The camera required an internal instead of an external position  
 250 because it was impossible to see the complete receiver front wall through the smaller cavity  
 251 aperture.

252 Two calibrations were needed to use the camera as a radiometric measurement device.

253 • Spatial calibration. A reference checkerboard was placed on the receiver in order to  
 254 determine the optical aberrations and the perspective effect due to the fisheye lens and the  
 255 installation of the camera inside the cavity. A simplified algorithm was used, as it was sufficient  
 256 to deliver the low-resolution flux map needed for the next steps (25x25 mm final resolution).

257 • Radiometric calibration. This was done using a reference radiometer sensor (Vatell  
 258 25 mm) installed at the center of the Lambertian receiver in the mockup cavity. This sensor  
 259 allowed the conversion from brightness (gray levels) to flux density measurements ( $\text{kW}/\text{m}^2$  or  
 260 suns). The brightness homogeneity of the fisheye lens was evaluated before this conversion  
 261 using diffuse lighting of the cavity, with the heliostats reflecting the solar radiation at the bottom  
 262 of the parabola (simplified white box setup).

263 The data processing steps are summarized in Figure 9. Thirty-five heliostats were selected to  
 264 establish the database based on their incident beam angle.



265

266

267

268

269

**Figure 9.** Sample case of the data processing of the flux measurement system with a fisheye lens for the aiming strategy determination: 1) spatial calibration by means of a reference checkerboard 2) radiometric calibration with the reference radiometer installed at the center of the receiver 3) data decimation to simplify the post processing and aiming strategy determination

270

271

272

273

274

275

276

277

278

279

280

281

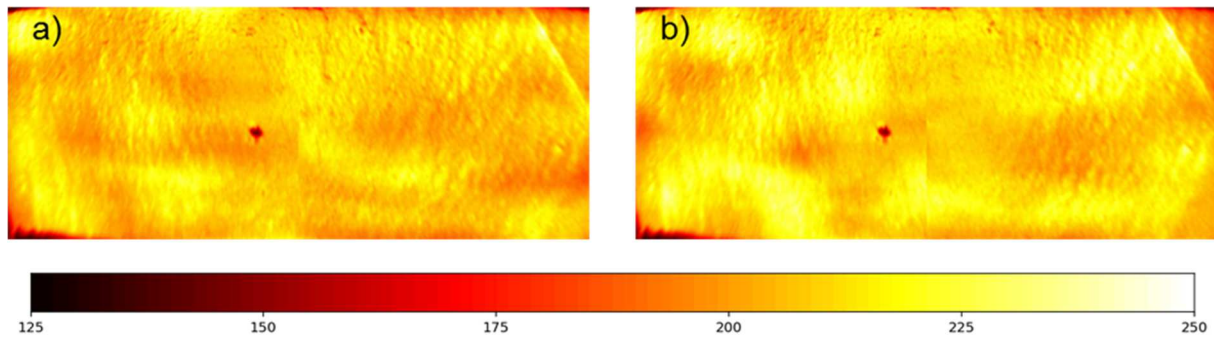
282

283

284

285

A genetic algorithm was selected and implemented to determine the best heliostat offset configurations using the experimental database. A large number of significantly different configurations with the best statistical performance were identified. The performance was evaluated with the mean flux level and the flux homogeneity on the receiver. Approximately 2000 configurations, for all flux levels, were finally considered, along with 3 different positions of the cavity aperture shutter. Even if the configurations discovered with the evolutionary algorithm exhibited a satisfactory homogeneity, the average thermal homogeneity on the receiver was further improved by cycling between different heliostat configurations that had similar statistical performances (mean and standard deviation) but different heliostat aiming configurations (temporal dithering). Since the location of the hot and cold spots differed between these configurations, changing the aiming configurations resulted in smoothing temperature difference over time to achieve better mean spatial and temporal average temperatures using the thermal inertia of the receiver. This was achieved by changing quickly between the configurations, every 15 seconds. As an example, two solar flux density distributions (processed images from the camera) that correspond to an average concentration of 215 suns are illustrated in Figure 10.



286

287

288

289

290

291

**Figure 10.** Distribution of the flux density of two heliostat configurations giving an average concentration factor ( $C$ ) of 215. a)  $139 < C < 237$  ( $\sigma = 12.5$ ). b)  $150 < C < 239$  ( $\sigma = 14.5$ ). The central point corresponds to the fluxmeter. The colormap is the OpenCV “hot” palette: from 125 suns (black) to 250 suns (white), with red (175 suns) and yellow (225 suns) in between.

### Particles

292

293

294

295

296

297

298

299

300

301

302

303

304

305

306

307

308

309

310

311

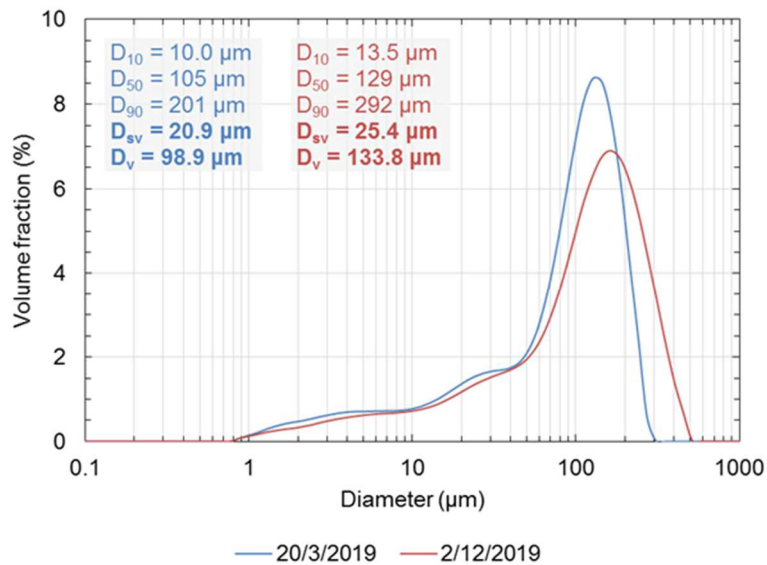
312

313

The decomposition of calcite aims to produce quicklime by removing the carbon dioxide:  $\text{CaCO}_3 \rightarrow \text{CaO} + \text{CO}_2$ . This calcination reaction typically occurs at approximately 850-950°C, depending on the  $\text{CO}_2$  partial pressure (the higher the  $\text{CO}_2$  partial pressure, the higher the temperature of reaction) (Valverde, 2015).

The calcite used during the tests was supplied by the company La Provençale from the quarry of Espira-del’Agly in France. This industrial feedstock was directly used without pretreatment. Measurements of the mass loss ratio after complete calcination of several samples (at 950 °C for 3 hours) showed that the fresh raw material consisted of 98.5% to 100%  $\text{CaCO}_3$ , with the remaining part consisting of nonreactive materials. In a conservative approach, a mass loss ratio corresponding to 98.5%  $\text{CaCO}_3$  was considered to calculate the degree of conversion.

The particle size distribution of the fresh raw material was analyzed twice during the test campaign. The results are reported in Figure 11. The results of the two measurements are not identical because of the variability of the raw material. In both cases, Figure 11 shows the relatively high fraction of fine particles (approximately 10% of the volume fraction with a diameter less than 10  $\mu\text{m}$ ). Considering the Sauter mean diameter  $d_{sv}$  of the particles and the density of calcite, which is 2710  $\text{kg/m}^3$ , the particles are classified as C-type particles (cohesive) according to the Geldart classification (Geldart, 1973). Indeed, this does not correspond to the experimental observations during the fluidization tests. Considering the average volume diameter  $d_v$  of the particles instead of the Sauter mean diameter, the particles are classified as between A-type (aeratable) and B-type (bubbling) particles. This corresponds better to the experimental observations.



314

315

**Figure 11.** Particle size distribution of the calcite used during the tests.

316

317 The minimum superficial fluidization velocity of the particles at ambient temperature and  
 318 pressure (~20 °C, 840 hPa) was measured experimentally. Three tests gave an average value  
 319 of 8.8 mm/s. By using the average evolution of the minimum fluidization velocity as a function  
 320 of the temperature predicted by several correlations from the literature ([Broadhurst and](#)  
 321 [Becker, 1975](#); [Thonglimp et al., 1984](#); [Wen and Yu, 1966](#)), it is possible to extrapolate the  
 322 measured value at high temperature. Thus, a minimum fluidization velocity of 8.8 mm/s at 20°C  
 323 corresponds to a minimum fluidization velocity of 4.0 mm/s at 800 °C. In addition, the  
 324 fluidization of the particles was tested in a transparent mockup of the solar reactor. These tests  
 325 resulted in determination of the minimum airflow rate that ensured a good circulation of the  
 326 particles. At ambient temperature, a fluidization flow rate corresponding to at least 5 times the  
 327 minimum fluidization velocity was required.

328

### 329 **3. Test results**

#### 330 *Operation procedure*

331

332 Typical solar tests lasted from four to six hours. A test consisted of two consecutive phases:  
 333 first, the reactor filled with particles was heated until the fluidized bed reached the temperature  
 334 of reaction; then, the reactor was fed with the appropriate mass flow rate of particles until a  
 335 steady state was reached. During the test, the critical operating parameter was the opening of  
 336 the cavity aperture. At the beginning of the heating period, the cavity's shutter was opened  
 337 progressively to avoid thermal shocks. Then, the shutter position was controlled to maintain  
 338 the indicated front wall temperature between 950 and 1050 °C. The position of the shutter was

339 adapted to compensate the daily variations of the direct normal irradiance (DNI) in order to  
340 maintain a stable temperature level on the reactor front wall and, consequently, inside the  
341 fluidized bed compartments. Stable chemical conversion of the fluidized particles was  
342 proportional to the mean residence time of the particles in the reactor,  $\tau$  (i.e., to the particle  
343 inlet mass flow rate). Consequently, when a stable particle temperature was maintained during  
344 the characteristic time  $\tau$ , the conversion degree at the reactor outlet reached the equilibrium  
345 value. In addition, the stability of the CO<sub>2</sub> content in the exhaust gases was a very sensitive  
346 indicator to assess the evolution of the calcination reaction.

347 The rigorous assessment of the steady-state regime could only be ascertained after the test,  
348 with the analysis of the particles sampled at the exit of the reactor. Obviously, steady-state  
349 regime corresponded to a constant degree of conversion in consecutive samples.

350 The degree of conversion of the samples taken at the reactor outlet was determined by  
351 complete calcination. The mass loss experienced by the sample after its complete calcination  
352 in an electrical furnace was compared to the mass loss experienced by a reference sample of  
353 initial particles taken at the reactor inlet. The complete calcination was carried out by heating  
354 the samples at 950 °C for 3 hours. The degree of conversion is given by Equation (1).

$$355 \quad \alpha = 1 - \frac{\frac{m_s - 1}{m_f}}{\frac{m_{ref,0} - 1}{m_{ref,f}}} \quad (1)$$

356 In this equation,  $m_s$  is the mass of the analyzed sample taken at the reactor outlet,  $m_f$  is the  
357 final mass of the sample after complete calcination in an electrical furnace,  $m_{ref,0}$  is the mass  
358 of a reference sample of raw calcite taken at the reactor inlet, and  $m_{ref,f}$  is the final mass of the  
359 reference sample after complete calcination in the electrical furnace.

### 360 *Experimental results*

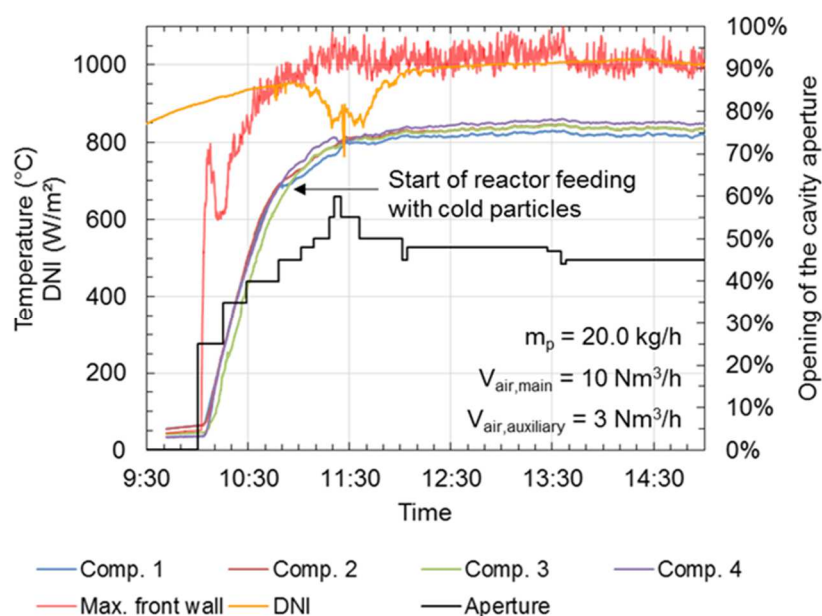
361 The effects of two main parameters, i.e., the fluidization conditions (air mass flow rate) and the  
362 particle mass flow rate, on the conversion degree was examined. One cannot consider the  
363 particle temperature as a parameter because it is the result of the constraint on the maximum  
364 acceptable wall temperature.

365 During the tests, particular attention was paid to the heating period of the reactor in order to  
366 reduce the time during which no calcination reaction occurred, as the particle temperature was  
367 too low. A key factor that governed the dynamic thermal behavior of the solar reactor was the  
368 fluidization velocity. Figure 12 plots the variations of the mean temperature in the four  
369 compartments of the solar reactor, the maximum temperature of the reactor's front wall, the  
370 degree of aperture of the solar cavity and the DNI with time for one typical experiment. The  
371 mean temperature in the compartments corresponds to the arithmetic average of the

372 temperature as measured by all the thermocouples immersed in the fluidized bed of particles  
373 (orange and green dots of Figure 5).

374 Figure 12 indicates that the heating period duration was less than one hour and that the  
375 temperature difference between the compartments was very small. The particles were injected  
376 approximately 45 min after the starting of the experiment, when the CO<sub>2</sub> analyzer indicated a  
377 significant increase in the CO<sub>2</sub> content in the flue gas. The equilibrium temperature was then  
378 reached after approximately 30 min.

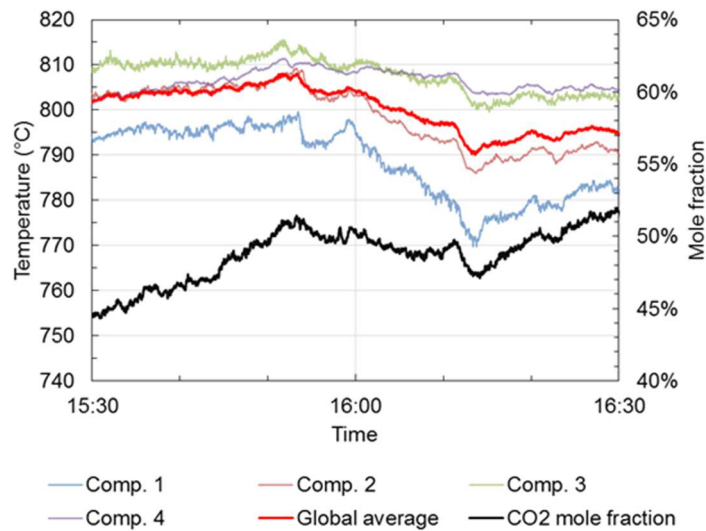
379 Figure 12 also shows how the mean particle temperature was maintained through the variation  
380 of the shutter position. The variation of DNI at 10:45 was compensated by the opening of the  
381 shutter that resulted in an increase of the solar power entering the cavity. The shutter was then  
382 gradually closed to follow the DNI increase.



383

384 **Figure 12.** Variations of main operation parameters with time during a typical experiment.

385 The sensitivity of the CO<sub>2</sub> analyzer to the fluidized bed temperature is illustrated in Figure 13.  
386 At the beginning of the sequence, the CO<sub>2</sub> mole fraction increases to reach the equilibrium  
387 value corresponding to the mean temperature (at approximately 15:50). Then, the CO<sub>2</sub>  
388 analyzer follows the variation of the temperature, resulting in the change of the calcination  
389 reaction kinetics.



390

391 **Figure 13.** Response of the CO<sub>2</sub> analyzer to the temperature variation of the four compartments of the  
 392 solar fluidized bed.

393 Table 1 lists the operation parameters and the main results of the six representative  
 394 experimental tests. The particle mass flow rate and the solar power varied from 14.5 to  
 395 25.1 kg/h and from 45.4 to 64.4 kW, respectively. The maximum degree of conversion was  
 396 95.2% at 20 kg/h and 57.8 kW (solar power). Surprisingly, the degree of conversion of the test  
 397 at 20 kg/h and low fluidization velocity exhibited a higher mean particle temperature but a lower  
 398 degree of conversion than the test at high fluidization velocity. Two phenomena may contribute  
 399 to this result: the CO<sub>2</sub> partial pressure and the insufficient mixing of particles. At low fluidization  
 400 flow rate, the CO<sub>2</sub> partial pressure in the reactor is higher than at high fluidization flow rate,  
 401 and the mixing of particles in the compartment is weak, resulting in a larger thermal gradient  
 402 inside the bed of particles. In particular, the particle temperature is much higher than the mean  
 403 temperature very near the irradiated wall, but the temperature is 100°C or more lower near the  
 404 back wall under these conditions. Both phenomena contribute to a lower degree of conversion,  
 405 even at a higher mean temperature.

406

Table 1. Main experimental results of the test campaign.

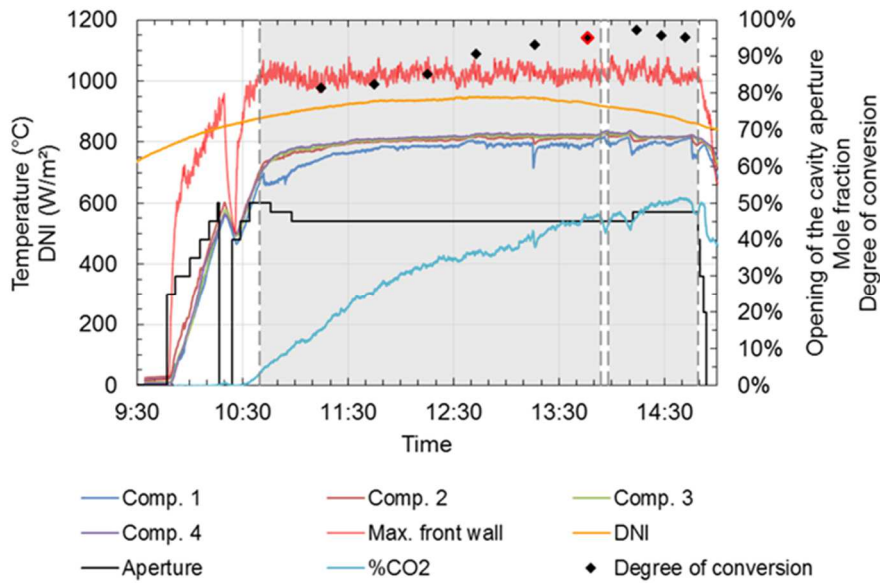
$F_p$ (kg/h)	$F_{air,main}$ (Nm <sup>3</sup> /h)	$F_{air,auxiliary}$ (Nm <sup>3</sup> /h)	DNI mean (W/m <sup>2</sup> )	C mean	Aperture	$P_{in}$ (kW)	$T_p$ (°C) Global average	$T_{w,max}$ (°C)	$\alpha_{out}$
14.5	10.1	0	970	220	33.0%	45.4	818	1108	94.1%
14.5	14.0	3	777	220	52.5%	58.4	813	972	90.8%
20.0	10.1	3	1000	220	48.0%	67.4	831	997	88.5%
20.0	19.3	4	927	220	45.0%	57.8	813	1022	95.2%
25.1	12.3	3	962	220	42.5%	55.9	790	949	40.5%

<b>25.1</b>	19.6	4	768	220	65.0%	64.4	804	1063	77.5%
-------------	------	---	-----	-----	-------	------	-----	------	-------

407

408 For each particle mass flow rate, two fluidization conditions (low and high fluidization velocity)  
409 have been tested. Because the other operation parameters could not be kept identical from  
410 one test to the other, the data do not enable clear identification of a single influence of the  
411 fluidization flow rate. However, during the tests, it was observed that increasing the fluidization  
412 flow rate improves the mixing and the circulation of the particles and hence the thermal  
413 homogeneity of the fluidized bed. Increased fluidization also improves the heat transfer  
414 coefficient of the particles and allows increased incident solar power on the reactor's front wall  
415 without overheating. Moreover, from a theoretical point of view, a high fluidization flow rate  
416 reduces the partial pressure of CO<sub>2</sub> in the fluidized bed and promotes the calcination reaction.  
417 However, at high fluidization flow rate, a larger proportion of the particles was recovered in the  
418 filter. This proportion was approximately 20% and 50% respectively at low and high fluidization  
419 flow rates. These relatively high proportions were probably caused by the undersizing and  
420 clogging of the cyclone. Consequently, for future applications, specific attention should be paid  
421 to the design of the dust extracting system.

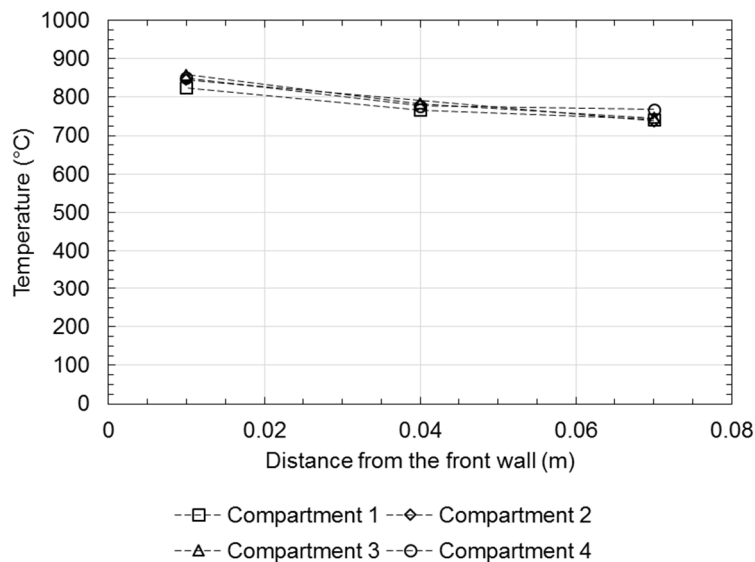
422 The next figures illustrate the test results. Figure 14 plots, for the best result (20 kg/h, high  
423 fluidization velocity), the time variation of the DNI, the compartment temperatures, the  
424 maximum front wall temperature, the CO<sub>2</sub> mole fraction, and the calcination degree. The  
425 calcination degree is not zero at the beginning of the test because the run started with the  
426 calcite-lime mixture resulting from the previous run. The chemical conversion stabilized  
427 approximately 2 h after the starting of particle feeding that corresponds to the mean residence  
428 time of the feedstock inside the reactor. The time during which the particles were fed in the  
429 reactor is shown in gray. The feeding was stopped after a few minutes, at 13:54, due to a minor  
430 technical problem. As a result, a small increase in the conversion degree was observed just  
431 after this event (97%); then it stabilized at the mean value (95%).



432

433 **Figure 14.** Time evolution of the operating parameters and results. Calcite 20.0 kg/h, high fluidization  
 434 flow rate. Gray area: feeding of the reactor with particles. Red dot: degree of conversion  
 435 corresponding to steady-state regime.

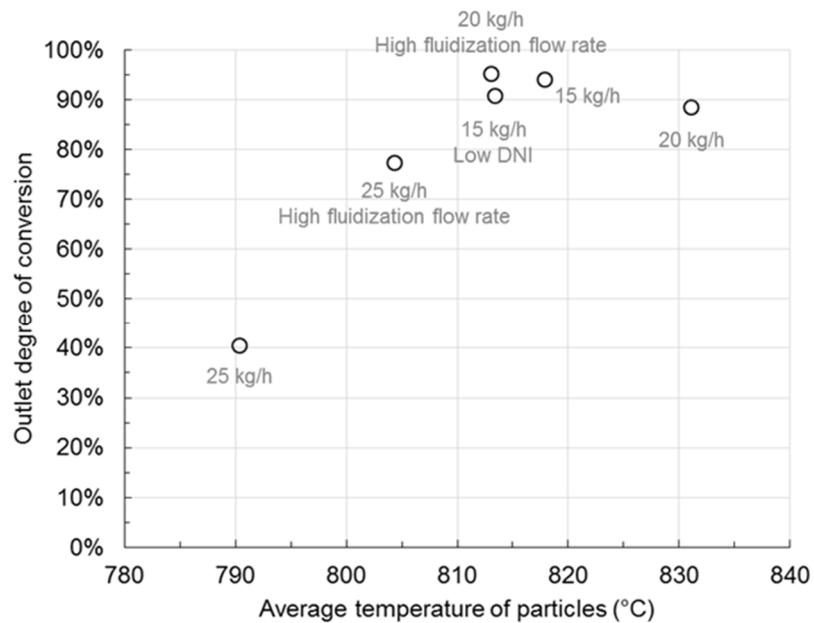
436 Figure 15 shows the temperature profile inside the compartments along the reactor depth  
 437 (8 cm). The mean temperatures and temperature profiles were very close in the four  
 438 compartments. The particle temperature near the front wall ranged from 825 °C to 858 °C, and  
 439 the maximum temperature difference was less than 115 °C between the front and back of the  
 440 fluidized bed. This result indicates the efficient mixing of the particles.



441

442 **Figure 15.** Temperature profile inside the fluidized particles. Calcite 20.0 kg/h, high fluidization flow  
 443 rate.

444 The inlet mass flow rate of particles influenced the mean residence time of the particles in the  
 445 reactor. From a theoretical point of view, the higher the residence time, the higher the outlet  
 446 degree of conversion. However, the results of the test campaign showed that the mass flow  
 447 rate of particles had a second-order influence on the outlet degree of conversion in the mass  
 448 flow rate range of 5-20 kg/h. The first-order parameter was the temperature, as illustrated in  
 449 Figure 16, which illustrates the variation of the degree of conversion with mean particle  
 450 temperature. In the temperature range tested, 790–832 °C, there is a strong effect of the global  
 451 average particle temperature (accounting for the four compartments) on the calcite conversion.  
 452 This result indicates the sensitivity of the reaction kinetics with temperature.



453  
 454 **Figure 16.** Degree of conversion of calcite (at steady state) as a function of the global average  
 455 temperature of the particles in the reactor.

456  
 457 **4. Result analysis**

458 The experimental study was completed with the analysis of the produced lime, reactor  
 459 thermal, and thermochemical performances.

460 The chemical composition of the product and BET surface area are listed in Table 2.

461  
 462  
 463  
 464

Table 2. Chemical and physical analysis of the produced lime (composition in mass fraction)

Composition/ Characteristics	15 kg/h	15 kg/h low DNI	20 kg/h low fluidization flow rate	20 kg/h high fluidization flow rate
CaO	90.52%	82.72%	80.65%	91.24%
CaCO <sub>3</sub>	8.45%	16.39%	18.60%	7.62%
CO <sub>2</sub>	3.72%	7.21%	8.18%	3.35%
SiO <sub>2</sub>	0.182%	0.141%	0.120%	0.140%
Fe <sub>2</sub> O <sub>3</sub>	0.061%	0.070%	0.050%	0.080%
Al <sub>2</sub> O <sub>3</sub>	0.131%	0.080%	0.090%	0.070%
MgO	0.514%	0.402%	0.450%	0.672%
MnO	0.002%	0.002%	0.002%	0.023%
S	0.001%	0.001%	0.002%	0.015%
$\alpha_{composition}$	94.9%	90.8%	88.3%	95.5%
$\alpha_{mass\ loss}$	94.1%	90.8%	88.5%	95.2%
SS (m <sup>2</sup> /g)	3.84	5.15	5.00	5.39

466

467 The chemical composition of the samples was determined by means of the X-ray fluorescence  
 468 method. The accuracy of this method is estimated to be  $\pm 1\%$ . The CO<sub>2</sub> mass fraction indicated  
 469 in Table 2 corresponds to the CO<sub>2</sub> present in the form of CaCO<sub>3</sub> and enables the validation of  
 470 the degree of calcination in the samples in addition to mass loss. The conversion degree  
 471  $\alpha_{composition}$  of the samples was calculated from the chemical composition. The uncertainties of  
 472 measurement of the conversion degree  $\alpha_{mass\ loss}$  calculated with the mass loss method is less  
 473 than  $\pm 2\%$  absolute. Considering these uncertainties, Table 2 indicates a very good agreement  
 474 between the degree of conversion obtained from the chemical composition and the mass loss.  
 475 In addition, the BET surface area is high (approximately 5 g/m<sup>2</sup>), indicating a high reactivity of  
 476 the product.

477 Two efficiencies are defined: The thermochemical efficiency ( $\eta_{thch}$ ) considers only the enthalpy  
 478 of reaction, while the thermal efficiency ( $\eta_{th}$ ) accounts for the enthalpy of reaction and the power  
 479 provided to heat the particles and the fluidization gases. They are defined as the ratio of these  
 480 values to the gross incident solar power through the cavity aperture ( $P_{in}$ ). The efficiencies are  
 481 calculated at steady state. The thermal power consumed to preheat the fluidization air is not  
 482 considered in the calculation because, in a commercial application, this power will be supplied  
 483 by recovering the waste heat of exhaust gases. Nevertheless, the increase of air enthalpy is

484 calculated using the inlet air temperature after the preheater. The efficiencies are defined as  
 485 follows:

$$486 \quad \eta_{\text{thch}} = \frac{P_{\text{reaction}}}{P_{\text{in}}} = \frac{x_{\text{CaCO}_3,0} \cdot \dot{m}_p \cdot \alpha_{\text{out}} \cdot M_{\text{CaCO}_3} \cdot \Delta H_{\text{R,CaCO}_3 \rightarrow \text{CaO} + \text{CO}_2}(T_{p,\text{mean}})}{P_{\text{in}}} \quad (2)$$

$$487 \quad \eta_{\text{th}} = \frac{P_{\text{reaction}} + \dot{m}_p \cdot h_{\text{CaCO}_3}^{T_{\text{in}} \rightarrow T_{p,\text{mean}}} + \dot{m}_{\text{air},\text{main}} \cdot h_{\text{air}}^{700^\circ\text{C} \rightarrow T_{p,\text{mean}}} + \dot{m}_{\text{air},\text{auxiliary}} \cdot h_{\text{air}}^{10^\circ\text{C} \rightarrow T_{p,\text{mean}}}}{P_{\text{in}}} \quad (3)$$

488 In these equations,  $x_{\text{CaCO}_3,0}$  is the mass fraction of calcium carbonate at the reactor inlet,  $\dot{m}_p$  is  
 489 the inlet mass flow rate of particles,  $\alpha_{\text{out}}$  is the degree of conversion measured at the reactor  
 490 outlet,  $M_{\text{CaCO}_3}$  is the molar mass of calcium carbonate (100.087 g/mol),  $T_{p,\text{mean}}$  is the average  
 491 temperature of particle in the reactor,  $P_{\text{in}}$  is the solar power entering the cavity,  $\dot{m}_{\text{air},\text{main}}$  and  
 492  $\dot{m}_{\text{air},\text{auxiliary}}$  are respectively the mass flow rates of the main and the auxiliary fluidization  
 493 airflows, and  $h^{T_1 \rightarrow T_2}$  is the difference of specific enthalpy between the temperatures  $T_1$  and  $T_2$ .  
 494 Then,

$$495 \quad \Delta H_{\text{R,CaCO}_3 \rightarrow \text{CaO} + \text{CO}_2} = -1.447 \cdot 10^{-6} \cdot T^3 + 3.323 \cdot 10^{-3} \cdot T^2 + 5.882 \cdot T + 1.810 \cdot 10^5 \quad (4)$$

$$496 \quad h_{\text{CaCO}_3}(T) = 9.963 \cdot 10^2 \cdot T + 1.345 \cdot 10^{-1} \cdot T^2 + 5.882 \cdot T + \frac{2.156 \cdot 10^7}{T} \quad (5)$$

$$497 \quad h_{\text{air}}(T) = 1.041 \cdot 10^3 \cdot T - 1.512 \cdot 10^{-1} \cdot T^2 + 2.500 \cdot 10^{-4} \cdot T^3 - 9.883 \cdot 10^{-8} \cdot T^4 + 6.782 \cdot$$

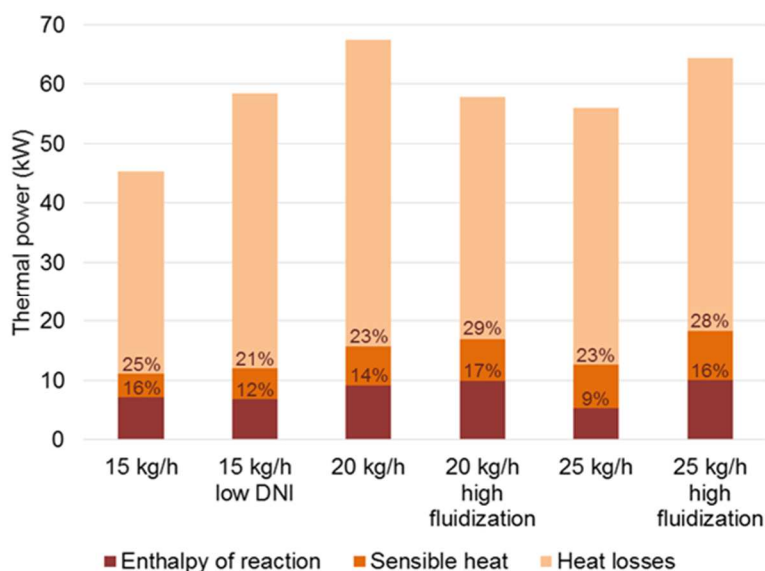
$$498 \quad 10^{-12} \cdot T^5 + 2.686 \cdot 10^{-15} \cdot T^6 \quad (6)$$

499 The enthalpy of the calcination reaction was calculated by assuming that the reaction occurred  
 500 in the whole reactor at the average temperature of particle. The enthalpy of reaction  $\Delta H_{\text{R}}$  is  
 501 given in Joule per mole of  $\text{CaCO}_3$  by Equation (4), with the temperature  $T$  expressed in Kelvin.  
 502 This formula was obtained by regression of the tabulated variations of enthalpy for the reaction  
 503  $\text{CaCO}_3 \rightarrow \text{CaO} + \text{CO}_2$ , calculated with the data from [Robie and Hemingway, 1995](#). For  
 504 example, this equation shows 0.525 kWh/kg of  $\text{CaCO}_3$  converted at 800 °C.

505 In Equations (5) and (6) the coefficients are respectively taken from [Robie and Hemingway,](#)  
 506 [1995, and Hilsenrath et al., 1955](#).

507 The solar power entering the cavity was calculated with data processing of measurements at  
 508 the cavity aperture. For each configuration of heliostats, the whole range of aperture degree  
 509 of the cavity was considered. The power was calculated every 5%, from 0% to 100% of  
 510 aperture, and interpolations were used in between. All the configurations of heliostats  
 511 potentially used during a test were simulated (due to the temporal dithering method, many  
 512 configurations are used during one single test). Then, the results were averaged in order to  
 513 obtain a mean solar power, depending on the concentration factor and the opening of the cavity  
 514 aperture (surface area of the aperture).

515 Figure 17 shows the distribution of the solar power entering the cavity between the power used  
 516 for the calcination reaction, the overall power transferred to the particles and the gas, and the  
 517 thermal losses. The data corresponded to steady state when the outlet degree of conversion  
 518 stabilized. The uncertainty on the data is estimated to be 10%. This power typically ranges  
 519 from 45 kW to 65 kW. Considering the inlet mass flow rate of particles and the outlet degree  
 520 of conversion, the heat consumed by the reaction typically ranges from 6.8 kW to 10.1 kW,  
 521 except for the test at 25 kg/h (in standard conditions), which exhibits a low degree of  
 522 conversion. Consequently, the calculated thermochemical efficiency ranges from 12% to 17%  
 523 (9% for the test at 25 kg/h). By considering the sensible heat provided to the particles and the  
 524 fluidization air, the total useful energy ranges from 11 kW to 18 kW. Consequently, the thermal  
 525 efficiency ranges from 21% to 29%. The enthalpy of reaction represents from 55% to 63% of  
 526 the useful energy (42% for the test at 25 kg/h).



527  
 528 **Figure 17.** Distribution of the solar thermal power entering the cavity and corresponding thermal and  
 529 thermochemical efficiencies at steady state.

530 Finally, the best result was obtained for a calcite mass flow rate of 20 kg/h, resulting in a degree  
 531 of conversion of 95.2%, a BET surface area of the lime of 5.39 m<sup>2</sup>/g, and 17% and 29%  
 532 thermochemical and thermal efficiency of the reactor, respectively.

### 533 5. Discussion

534 This section presents comments on the applications of lime and quality standards, the  
 535 management of CO<sub>2</sub>, and scaling-up issues of the solar process.

536 Applications of lime are broad, and the relative importance of each industry varies heavily from  
 537 one country to another. The main application domains are the iron and steel industry,

538 environmental protection, construction materials, civil engineering, the chemical industry, and  
539 agriculture. For example, 40% of lime in Europe is used in the steel industry (EuLA, 2020). It  
540 is obvious that lime quality criteria depend on the application domain. Expected properties are  
541 chemical purity, color, reactivity with water and gases (quicklime), mechanical behavior (in  
542 particular compressive strength), mean particle size, particle size distribution, and others. The  
543 standard for CaO content in the product is not the same for applications in the steel industry  
544 as it is for construction materials. The mean CaO content is 95% (93% minimum) for steel  
545 making, approximately 92% for water treatment, and 98% for construction materials (Oates,  
546 1998). Specific standards have been published in each application domain. For example, the  
547 EN 459-2 standard defines the test to measure quicklime reactivity for construction  
548 applications.

549 Lime reactivity depends on material porosity and BET specific surface area. Commandré et al.  
550 (2007) reported a complete study of lime reactivity as a function of calcination temperature and  
551 CO<sub>2</sub> partial pressure. They showed that the reactivity varies dramatically with both parameters.  
552 Lime produced at 600 °C and 750 °C in laboratory conditions under nitrogen exhibited a  
553 specific surface area of 80 m<sup>2</sup>/g and 30 m<sup>2</sup>/g, respectively. Heating the sample up to 1100 °C  
554 caused a reduction of the surface area to 1.65 m<sup>2</sup>/g and 1.15 m<sup>2</sup>/g under N<sub>2</sub> and CO<sub>2</sub>,  
555 respectively. The loss in reactivity due to CO<sub>2</sub> partial pressure is known as “chemical sintering,”  
556 which is similar to thermal sintering due to temperature. In industrial lime kilns, the feedstock  
557 experiences temperature in the range of 1100-1300 °C that results in sintering of the product.  
558 Consequently, BET surface areas of limes produced by shaft kilns and rotary kilns are less  
559 than 1 m<sup>2</sup>/g and 2 m<sup>2</sup>/g respectively. Fluidized bed kilns only produce lime with specific surface  
560 areas equal or larger than 2 m<sup>2</sup>/g because they operate at lower temperatures. This type of  
561 quicklime is named “highly reactive” (Dheilly et al., 1998).

562 Carbon dioxide content in the reactor during calcination appears to be a key process  
563 parameter. On the one hand, increasing the CO<sub>2</sub> partial pressure results in a decrease of the  
564 calcination kinetics at a given temperature and a reduction of product reactivity. On the other  
565 hand, it should be of interest to operate under 100% CO<sub>2</sub> in order to produce a pure CO<sub>2</sub> flue  
566 gas that can be sequestered and used in the chemical industry. The fluidized bed technology  
567 allows a choice of the operation conditions that fit with the targeted application because  
568 fluidization gas can be changed from air to CO<sub>2</sub>. Consequently, the choice of the operation  
569 conditions is a result of a compromise between solid product properties and utilization of  
570 process gas.

571 This paper demonstrates the capacity of multistage horizontal fluidization to achieve pilot-scale  
572 calcination of limestone in continuous mode. The next step will be the scaling up of the

573 technology to the MW scale with a reactor efficiency similar to that of industrial kilns. In  
574 commercial lime kilns, the feedstock (limestone,  $\text{CaCO}_3$ ) is heated from ambient temperature  
575 to above 800 °C in the preheating zone by the gas leaving the calcination zone. This  
576 corresponds to the internal heat recovery. The overall heat requirement for the process  
577 (heating and chemical reaction) is 4900 kJ/kg CaO, with two-thirds (62%) corresponding to the  
578 calcination reaction. The thermochemical efficiency (100% corresponding to a heat  
579 consumption of 3060 kJ/kg CaO) of commercial lime kilns was discussed in [Oates \(1998\)](#). This  
580 efficiency varies strongly with the type of kiln. For long rotary kilns, it ranges from 40 to 50%,  
581 while it reaches 77-90% for modern shaft kilns. Fluidized bed industrial lime kilns exhibit a  
582 medium thermochemical efficiency of approximately 60%. The challenges concerning heat  
583 recovery differ widely between the standard and the solar kilns. In standard lime kilns, the  
584 exhaust gas contains more heat than is required to preheat the feedstock, and the product  
585 (lime) does not contain enough energy to preheat the combustion air ([Oates, 1998](#)). In the  
586 solar kiln, the exhaust gas does not contain enough energy to preheat the feedstock but  
587 contains more heat than is necessary to preheat the fluidization gas. Consequently, it is  
588 necessary to recover heat from the hot product in order to preheat both the limestone and the  
589 fluidization gas. Heat recovery from the hot product can be performed in a secondary fluidized  
590 bed located at the exit of the solid product (lime outlet). The produced hot air from this direct  
591 contact heat exchanger and the exhaust gas from the solar reactor is used for the preheating  
592 of both the limestone and the fluidization air.

593 A demo-scale (MW scale) fluidized bed calcination solar reactor can target a thermochemical  
594 efficiency similar to an industrial fossil-fueled fluidized bed kiln (approximately 60%), using heat  
595 recovery as explained in the previous paragraph. A cavity-type solar reactor operating with an  
596 irradiated wall at 1000 °C and an irradiated surface area and aperture surface area ratio of 2  
597 experiences 30% radiation loss (dominant mode of heat loss). This accounts for our  
598 experimental results that reveal the mean solar flux density on the reactor wall will be  
599 approximately 250 kW/m<sup>2</sup> and the mean solar flux density at the aperture will be 500 kW/m<sup>2</sup>.  
600 The MW-scale solar reactor will consist of the assembly of four 1x1 m single-stage fluidized  
601 bed modules working in series. This design allows the same residence time distribution of  
602 particles that was achieved in the pilot-scale solar reactor. At commercial scale, a 40 MW solar  
603 reactor can produce 300 tons/day of quicklime. Considering the application of the solar  
604 technology at an industrial scale, two issues must be considered: maintaining product quality  
605 (conversion degree) and designing a 24 h-per-day process. The former issue can be  
606 addressed by adding a maturing reactor in series with the solar reactor. This reactor can be  
607 heated by fuel since the energy requirement is very small with respect to the solar part. The  
608 latter issue can be addressed by the implementation of a hybrid process in which the thermal

609 energy is provided by concentrated solar and combustion heat sources. Clean combustion  
610 heat sources can be either hydrogen or biomethane. In addition to lime production, the fluidized  
611 bed solar technology can be applied to thermochemical energy storage, since this calcination  
612 process produced highly reactive quicklime.

613

## 614 **6. Conclusion**

615 This paper demonstrates the successful scaling up of the horizontal multistage solar fluidized-  
616 bed concept at pilot scale for calcination. The on-sun operation of the system with a mean flux  
617 density of 220 suns indicates the sensitivity of the reactor to the fluidization conditions and the  
618 solar flux distribution on the solar-irradiated wall. The efficient mixing of fluidized particles  
619 results in an effective wall-to-fluidized bed heat transfer that allows a mean wall-to-particle  
620 temperature difference of approximately 100°C and a temperature gradient of approximately  
621 10°C/cm along the bed width. Moreover, the separation of the reactor in four sections narrows  
622 the residence time distribution of the particles. As a result, the product quality is constant and  
623 the conversion degree is high when a steady state is reached. For example, a conversion  
624 degree of 95% was obtained for a calcite mass flow rate of 20 kg/h and a mean overall bed  
625 temperature of 815°C. This achievement corresponds to a particle mass flow rate three times  
626 higher than the current state of the art for solar calcination. The next target is the demonstration  
627 of a 1-MW solar reactor operating either in solar-only mode (daytime) or in hybrid mode (24 h  
628 per day).

629

## 630 **Acknowledgements**

631 This project has received funding from the European Union's Horizon 2020 research and  
632 innovation program under grant agreement No. 654663, SOLPART project.

633 This work was supported by the French Investments for the Future program managed by the  
634 National Agency for Research under contract "ANR-10-EQPX-49-SOCRATE" (Equipex  
635 SOCRATE).

636 The authors thank Philippe Dumont (NLD) for providing the chemical analysis of the samples.

637

## 638 **References**

639 Broadhurst, T.E., Becker, H.A., 1975. Onset of fluidization and slugging in beds of uniform  
640 particles. *AIChE Journal* 21, 238–247. <https://doi.org/10.1002/aic.690210204>

641 Comessa, Thermal processing of bulk solids, [www.comessa.com](http://www.comessa.com).

642 Commandre J-M., Salvador S., Nzihou A. (2007). Reactivity of laboratory and industrial  
643 limes. *Chemical Engineering Research and Design*, 85 (4): 473-480. [10.1205/cherd06200;](https://doi.org/10.1205/cherd06200;hal-01634390)  
644 [hal-01634390](https://doi.org/10.1205/cherd06200;hal-01634390)

645 Dheilly, R.M., Tudo, J. and Queneudec, M., 1998, Influence of climatic conditions on the  
646 carbonation of quicklime, *Journal of materials, Engineering and Performance*, 7(6): 789–795.

647 Esence, T., Benoit, A., Poncin, D., Tessonnaud, M., Flamant, G., 2020. A shallow cross-  
648 flow fluidized-bed solar reactor for continuous calcination processes. *Solar Energy* 196, 389-  
649 398. <https://doi.org/10.1016/j.solener.2019.12.029>

650 EuLA, 2020, <https://www.eula.eu/>

651 Flamant, G., Hernandez, D., Bonet, C., Traverse, J.-P., 1980. Experimental aspects of the  
652 thermochemical conversion of solar energy; Decarbonation of CaCO<sub>3</sub>. *Sol. Energy* 24, 385–  
653 395. [https://doi.org/10.1016/0038-092X\(80\)90301-1](https://doi.org/10.1016/0038-092X(80)90301-1)

654 Fletcher, E. A. and Moen, R. L., 1977. “Hydrogen- and oxygen from water,” *Science*  
655 197(4308), 1050–1056.

656 Geldart, D., 1973. Types of gas fluidization. *Powder Technology* 7, 285–292.  
657 [https://doi.org/10.1016/0032-5910\(73\)80037-3](https://doi.org/10.1016/0032-5910(73)80037-3)

658 Hilsenrath, J., Beckett, C.W., Benedict, W.S., Fano, L., Hoge, H.J., Masi, J.F., Nuttall, R.L.,  
659 Touloukian, Y.S., Woolley, H.W., 1955. *Tables of Thermal Properties of Gases, Comprising*  
660 *Tables of Thermodynamic and Transport Properties of Air, Argon, Carbon Dioxide, Carbon*  
661 *Monoxide Hydrogen, Nitrogen, Oxygen, and Steam (Circular No. 564)*. U.S. Department of  
662 Commerce, National Bureau of Standards.

663 Imhof, A., 2000. Calcination of limestone in a solar reactor. *ZKG Int.* 53, 504–509.

664 Imhof, A., 1997. Decomposition of limestone in a solar reactor. *World Renew. Energy Congr.*  
665 *IV Renew. Energy Energy Effic. Environ.* 10, 239–246. [https://doi.org/10.1016/0960-](https://doi.org/10.1016/0960-1481(96)00072-9)  
666 [1481\(96\)00072-9](https://doi.org/10.1016/0960-1481(96)00072-9)

667 Li, L., Coventry, J., Bader, R., Pye, J., and Lipiński, W., 2016. Optics of solar central receiver  
668 systems: a review. *Optics Express*, Vol. 24, No. 14, A985- A1007.  
669 <https://DOI:10.1364/OE.24.00A985>.

670 Meier, A., Bonaldi, E., Cella, G.M., Lipinski, W., Wuillemin, D., 2006. Solar chemical reactor  
671 technology for industrial production of lime. *Sol. Energy* 80, 1355–1362.

672 Moumin G., Tescari S., Sundarraj P., de Oliveira L., Roeb, M., Sattler C., 2019 Solar  
673 treatment of cohesive particles in a directly irradiated rotary kiln. *Sol. Energy* 182, 480–490.  
674 <https://doi.org/10.1016/j.solener.2019.01.093>

675 NF EN 459-2, 2012, Construction lime, Part 2: Test method.

676 Nikulshina, V., Halmann, M., Steinfeld, A., 2009. Coproduction of Syngas and Lime by  
677 Combined CaCO<sub>3</sub>-Calcination and CH<sub>4</sub>-Reforming Using a Particle-Flow Reactor Driven by  
678 Concentrated Solar Radiation. *Energy Fuels* 23, 6207–6212.  
679 <https://doi.org/10.1021/ef9007246>

680 Oates, J.A.H., 1998. *Lime and Limestone: Chemistry and Technology, Production and Uses*.  
681 Wiley-VCH.

682 Olivier, J.G.J., Janssens-Maenhout, G., Muntean, M., Peters, J.A.H.W., 2016. Trends in  
683 global CO<sub>2</sub> emissions: 2016 Report. PBL Netherlands Environmental Assessment Agency

684 Robie, R.A. and Hemingway, B.S., 1995. *Thermodynamic Properties of Minerals and Related*  
685 *Substances at 298.15 K and 1 Bar (10<sup>5</sup> Pascals) Pressure and at Higher Temperatures*,  
686 U.S. Geological Survey Bulletin.

687 Steinfield, A., Imhof, A., Mischler, D., 1991. Experimental Investigation of an Atmospheric-  
688 Open Cyclone Solar Reactor for Solid-Gas Thermochemical Reactions. *J. Sol. Energy Eng.*  
689 *Trans. ASME* 114, 171–174. <https://doi.org/10.1115/1.293000>

690 Thonglimp, V., Hiquily, N., Laguerie, C., 1984. Vitesse minimale de fluidisation et expansion  
691 des couches fluidisées par un gaz. *Powder Technology* 38, 233–253.  
692 [https://doi.org/10.1016/0032-5910\(84\)85006-8](https://doi.org/10.1016/0032-5910(84)85006-8)

693 Touloukian, Y.S., Dewitt, D.P., 1970. *Thermal Radiative Properties: Metallic Elements and*  
694 *Alloys*, Purdue Research Foundation. ed, *Thermophysical Properties of Matter*. New York -  
695 Washington.

696 Tregambi, C., Salatino, P., Solimene, R., Montagnaro, F., 2018. An experimental  
697 characterization of Calcium Looping integrated with concentrated solar power. *Chem. Eng. J.*  
698 331, 794–802. <https://doi.org/10.1016/j.cej.2017.08.068>

699 Valverde, J.M., 2015. On the negative activation energy for limestone calcination at high  
700 temperatures nearby equilibrium. *Chem. Eng. Sci.* 132, 169–177.  
701 <https://doi.org/10.1016/j.ces.2015.04.027>

702 Wen, C.Y., Yu, Y.H., 1966. A Generalized Method for Predicting the Minimum Fluidization  
703 Velocity. *AIChE Journal* 12, 610–612. <https://doi.org/10.1002/aic.690120343>

